npj | 2D Materials and Applications www.nature.com/npj2dmaterials

ARTICLE OPEN

Photon-generated carrier transfer process from graphene to quantum dots: optical evidences and ultrafast photonics applications

X. Wang[1,6], X. H. Li[2,6], C. Jiang[1], C. T. A. Brown[3], J. Q. Ning[1], K. Zhang[4], Q. Yu[4], X. T. Ge[1], Q. J. Wang[5] and Z. Y. Zhang[1] ✉

Graphene/III–V semiconductor van der Waals (vdW) heterostructures offer potential access to physics, functionalities, and superior performance of optoelectronic devices. Nevertheless, the lack of a bandgap in graphene severely restricts the controllability of carrier properties and therefore impedes its applications. Here, we demonstrate the engineering of graphene bandgap in the graphene/GaAs heterostructure via C and Ga exchange induced by the method of femtosecond laser irradiation (FLI). The coupling of the bandgap-opened graphene with GaAs significantly enhances both the harvest of photons and the transfer of photon-generated carriers across the interface of vdW heterostructures. Thus, as a demonstration example, it allows us to develop a saturable absorber combining a delicately engineered graphene/GaAs vdW heterostructure with InAs quantum dots capped with short-period superlattices. This device exhibits significantly improved nonlinear characteristics including <1/3 saturation intensity and modulation depth 20 times greater than previously reported semiconductor saturable absorber mirrors. This work not only opens the route for the future development of even higher performance mode-locked lasers, but the significantly enhanced nonlinear characteristics due to doping-induced bandgap opening of graphene by FLI in the vdW heterostructures will also inspire wide applications in photonic and optoelectronic devices.

npj 2D Materials and Applications (2020)4:27 ; https://doi.org/10.1038/s41699-020-00160-6

INTRODUCTION

Owing to enhanced light harvesting and efficient rectifying behaviors, van der Waals (vdW) heterostructures combining atomically thin graphene and III–V semiconductors have emerged as a promising candidate to improve the performance of optoelectronic devices including solar cells, photodetectors, and light-emitting diodes[1–10]. However, due to the lack of a bandgap in graphene, the very weak transfer process of photon-generated carriers from graphene to the semiconductor in the vdW heterostructures imposes a challenge to achieve expected electrical and optoelectronic properties[11,12], which in turn limits widespread applications of this kind of vdW structures in such fields as ultrafast photonics.

Graphene has previously been demonstrated as an effective saturable absorber (SA) for mode-locked pulse generation due to its ultrabroad absorption spectrum and ultrafast recovery time[13], but poor operation stability inhibits its practical applications[14,15]. On the other hand, following the demonstration of III–V InGaAs quantum dot (QD) lasers[16], tremendous progress has been made in high performance active QD laser diodes (LDs) and passive ultra-fast lasers based on QD semiconductor saturable absorber mirrors (SESAMs)[17–23]. The emitting wavelength of the major QD devices, however, is generally around 1.3 µm. Recently, a QD-SESAM comprised of an asymmetric 1.55 µm InGaAs dot in well (DWELL) structure has been reported to realize a 10 GHz mode-locked solid state laser emitting at 1.55 µm with low saturation fluence of 15.7 MW cm^{-2}, but the achieved pulse width is limited to only ~2 ps due to the small modulation depth of ~0.4%[24]. Therefore, it is still desirable to explore techniques to increase the modulation depth of QD-SESAM for the development of femtosecond pulsed lasers with long stability.

Combining graphene with other materials to form vdW heterostructures has been proved to be an effective way to increase the modulation depth of a SA structure. For example, the tunable saturation fluence and modulation depth for transition metal dichalcogenides can be realized by capping with different layers of graphene due to tailored transfer of photon-generated carriers[25]. Nevertheless, non-uniform contact in graphene vdW heterostructures reduces the performance of hybrid SAs, which can be effectively optimized by laser irradiation. In this paper, we demonstrate the bandgap engineering of graphene in the graphene/III–V semiconductor vdW heterostructures with the technique of femtosecond laser irradiation (FLI) and investigate the underlying physical mechanism of the carrier transfer across the graphene/GaAs heterostructures. A series of SAs based on graphene/III–V semiconductor vdW heterostructures has been developed, with which a femtosecond mode-locked ultrafast laser emitting at 1.55 µm has been constructed. The 1.55 µm SA is comprised of a graphene/GaAs vdW heterostructure and a single layer QDs capped with $(In_xGa_{1-x}As/In_yGa_{1-y}As)_5$ short-period superlattices (SSLs). This structure exhibits superior optical characteristics to previously reported SESAMs[26]. Both simulation and experimental results indicate that a bandgap of 0.31 eV is created in graphene due to the C and Ga atoms exchange at the heterostructure induced by FLI, which is responsible for the enhanced photon collection efficiency and the carrier transfer efficiency across the graphene, and the III–V semiconductor interface.

[1]Key Laboratory of Nanodevices and Applications, Suzhou Institute of Nano-Tech and Nano-Bionics, Chinese Academy of Sciences, 215123 Suzhou, China. [2]School of Physics and Information Technology, Shaanxi Normal University, 710062 Xi'an, China. [3]SUPA, School of Physics and Astronomy, University of St Andrews, St Andrews, Fife KY16 9SS, UK. [4]i-Lab, Suzhou Institute of Nano-Tech and Nano-Bionics, Chinese Academy of Sciences, 215123 Suzhou, China. [5]Center for OptoElectronics and Biophotonics, School of Electrical and Electronic Engineering, Nanyang Technological University, 50 Nanyang Ave., Singapore 639798, Singapore. [6]These authors contributed equally: X. Wang, X. H. Li. ✉email: zyzhang2014@sinano.ac.cn

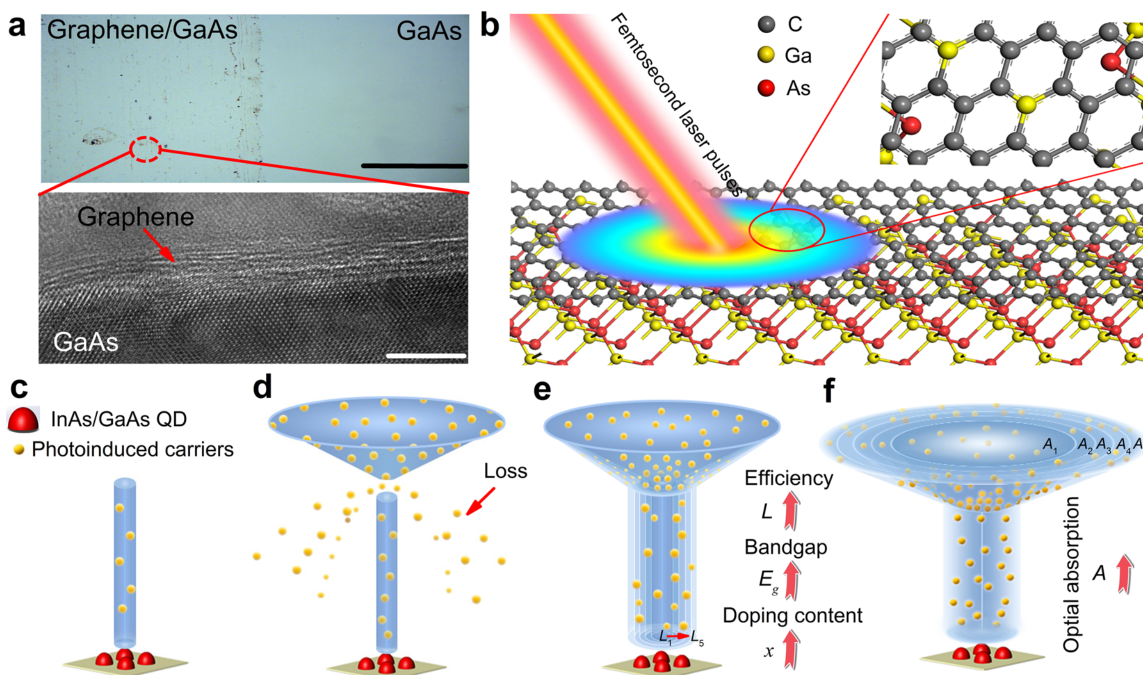

Fig. 1 Transfer process of the photo-generated carriers. a Optical image of graphene transferred onto a GaAs substrate and the cross-sectional TEM image of the interface of the graphene/GaAs vdW heterostructure. The scale bars used in the optical image and the cross-sectional TEM image are 10 μm and 5 nm, respectively. **b** The exchange of C and Ga or As atoms at the graphene/GaAs vdW heterostructure induced by FLI. **c**–**f** The illustration of different transfer processes for the photo-generated carriers for **c** InAs/GaAs QDs, **d** the non-irradiated graphene/GaAs vdW heterostructure, **e** the graphene/GaAs vdW heterostructure irradiated increasing power densities of femtosecond laser pulses, and **f** the graphene/GaAs vdW heterostructure capped with the different layers of graphene, where the funnel depicts the enlarged photon harvest and carrier generation by graphene, L_1–L_5 describe increasing carrier transfer efficiencies caused by the FLI, and A_1–A_5 represent the optical absorption of the graphene with increased layer numbers.

The SSL structure serves as a carrier reservoir to effectively adjust the carrier transfer dynamics, and the QDs are the final absorber of the photon-generated carriers. An Er-doped fiber laser constructed with the graphene/GaAs/SSL/QD SA exhibits continuously stable mode-locking, which is vastly superior to reported mode-locked lasers based on conventional QD-SESAMs, graphene, or other two-dimensional material-based SAs. The development of the doped-graphene/III–V semiconductor heterostructure SAs paves a way towards the realization of robust and high-performance ultrafast lasers which are of key importance for applications of all-optical clocking recovery, optical frequency comb, and coherent optical communication systems[27–29].

RESULTS

Carrier transfer process in vdW heterostructures

Figure 1a shows the optical image of the graphene/GaAs vdW heterostructures, which were fabricated by wet-chemical transfer of graphene layers onto the surface of a GaAs substrate and the cross-sectional transmission electron microscope (TEM) image of the graphene/GaAs heterostructure after a 740 nm femtosecond Ti:sapphire laser irradiation, where the closed contact at the interface can be observed clearly. Upon irradiating the graphene/GaAs vdW heterostructure with ultrashort laser pulses, the exchange between C and Ga or As atoms at the interface results in the doping of exotic atoms into the graphene lattice, as depicted in Fig. 1b. This doping induces the opening of an energy gap in the electronic structure of graphene, which could promote the transfer of photo-generated carriers from graphene to GaAs. The detailed comparison of these effects on the carrier transfer, including the power density of irradiating laser and the layers of graphene coated in the vdW heterostructures, are schematically presented in Fig. 1c–f. By comparing Fig. 1c, d, although enhanced photon harvesting and carrier generation are expected with graphene, the direct coating of graphene onto the InGaAs/GaAs QD structure can hardly result in the efficient transfer of carriers to reach the QDs, due to the severe carrier loss at the interface. As illustrated in Fig. 1e, the FLI treatment modifies the graphene/GaAs vdW interface and effectively enhances the carrier transfer, which leads to an adjustable transfer efficiency (L_1–L_5) of carriers across the heterostructures. In addition, as represented by the geometry size of the funnel top in Fig. 1f, the effects of optical absorption and carriers harvesting (A_1–A_5) could be controlled by varying the number of graphene layers in the graphene/GaAs vdW heterostructures, which is confirmed by the results of photo-luminescence (PL) and nonlinear reflection measurements.

Raman spectra of the vdW heterostructures treated with FLI

Raman spectroscopy is an efficient method for the characterization of graphene, doped graphene, and graphene-based vdW heterostructures due to the sensitive dopant and carrier effects on Raman vibrational modes[30,31]. The Raman spectra of the fabricated graphene/GaAs vdW heterostructures with different graphene layers are presented in Supplementary Fig. 1. The pristine mono-layer graphene exhibits two clear Raman peaks at ~1584 and 2676 cm^{-1} corresponding to the G band and 2D band, respectively. Mono-layer, tri-layer, and five-layer graphene in our samples were identified by the intensity ratio between G band and 2D band, respectively. To realize a closed contact of graphene with the GaAs substrate, the graphene/GaAs heterostructure was irradiated with a Ti:sapphire femtosecond pulsed laser at different power densities varied from 38.2 to 61.6 MW cm^{-2}. Figure 2a illustrates the irradiating power density at selected positions, and the corresponding optical image of the irradiated areas is shown in Fig. 2b. The distance among the areas irradiated with the same power densities of the femtosecond laser is about 2 μm, and the

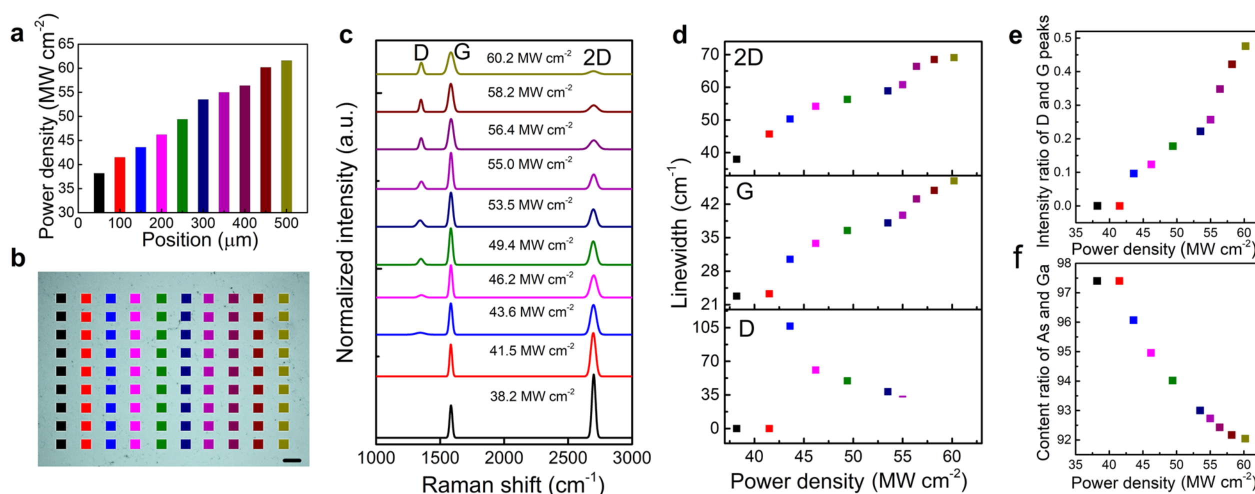

Fig. 2 Raman measurements of the vdW heterostructure. **a** Power density distributions of the femtosecond laser for irradiating the graphene/GaAs vdW heterostructure. **b** Power density distributions of the femtosecond laser on the surface of the irradiated graphene/GaAs vdW heterostructure. The scale bar used is 3 μm. **c** Raman spectra of the graphene/GaAs vdW heterostructure irradiated by femtosecond laser with different power densities. **d**, **e** The irradiation power density-dependent **d** linewidths and **e** intensity ratio of Raman spectra for the irradiated graphene/GaAs vdW heterostructure. **f** The irradiation power density-dependent content ratio of As and Ga for the irradiated graphene/GaAs vdW heterostructure measured by EDS.

distance among the areas irradiated with the different power densities of the femtosecond laser is about 3 μm.

The Raman spectra of the graphene/GaAs heterostructure treated with FLI at different power densities are presented in Fig. 2c. The Raman spectra of the mono-layer graphene/GaAs heterostructure remain the same as the non-irradiated sample until the irradiation laser power density exceeds 43.6 MW cm^{-2}. With the increase of the power density from 43.6 to 60.2 MW cm^{-2}, the third Raman peak at 1344 cm^{-1} gradually appears and becomes stronger. In addition, the linewidths of the D band become narrower, while those of the G band and 2D band become wider, and the intensity ratio between the D band and G band increases with the increased laser power density, as shown in Fig. 2d, e. Further increasing the FLI power density above 60.2 MW cm^{-2}, no obvious change in the Raman peaks can be observed, which can be attributed to the serious thermal damage to the graphene. It is well known that the D band of the graphene is related to the breathing mode of the six-atom rings; the G band is associated with the in-plane stretching mode of C–C bonds, and the 2D band corresponds to a phonon resonance mode[32]. In this work, when the power density is lower than 43.6 MW cm^{-2}, the energy of the femtosecond laser pulses is below the threshold to break the C–C bonds. As a result, the D band is not observed and the G band and 2D band are similar to those of the non-irradiated graphene. When the power density gets higher than 43.6 MW cm^{-2}, the C–C bonds are broken, leading to the quick broadening of the G band and 2D band, and the observation of the breathing mode-related D band. When the laser power density is much higher than 43.6 MW cm^{-2}, the decomposition of the underlying GaAs even occurs, which is confirmed by the energy-disperse spectroscopy (EDS) characterizations shown in Fig. 2f, manifested as the gradual decrease of the As elements with the increased FLI power density. This result suggests the possibility of intermixing C atoms with the atoms from GaAs.

FLI-induced bandgap opening in graphene

To investigate the graphene doping behavior as well as the carrier generation and transfer characteristics at the graphene/GaAs interface, a Schottky infrared photodetectors (SIPs) were fabricated with a single layer of graphene transferred onto the GaAs (Fig. 3a). A built-in electric field exists at the graphene/GaAs interface leading to the bending of the GaAs electron bands near the interface. Upon light illumination, electrons are excited in the graphene and migrate to GaAs driven by the built-in electric field to produce photocurrent and the holes accumulate at the surface of graphene[33]. The *I*–*V* curves of the device illuminated with 1550 nm light ranging from 0 to 197 μW are presented in Fig. 3b. An efficient rectifying behavior with applied bias is observed and the direction of photocurrent from GaAs to graphene is confirmed by the negative circuit current. According to the *I*–*V* curve obtained in darkness, the conduction band offset (ΔE_C) is calculated to be 0.61 eV by using the thermionic-emission theory[33]. The SIP device with the graphene/GaAs heterostructure was irradiated with a Ti:sapphire femtosecond pulsed laser at different power densities. It is found that, below 43.6 MW cm^{-2}, the photocurrent density (J) and ΔE_C remain the same as the non-irradiated samples, indicating the existence of a "threshold" of the graphene doping. As described in Fig. 1e, for the device treated with increased power density above 43.6 MW cm^{-2}, the J increases gradually, indicating enhanced carrier transfer efficiency. Irradiation densities of larger than 60.2 MW cm^{-2} lead to thermal damage to the vdW heterostructure. Figure 3c shows *I*–*V* curves of the SIP device irradiated at a 56.4 MW cm^{-2}, revealing a ΔE_C value of 0.51 eV which is much smaller than the non-irradiated heterostructure. It should be noted that, at the incident power of 197 μW and at zero bias voltage, the obtained J of the irradiated graphene/GaAs heterostructure is about 20 times larger than the non-irradiated sample, confirming a significantly enhanced light harvesting and carrier transfer due to the bandgap opening in the graphene.

Figure 3d, g show the valence band spectra of highly oriented pyrolytic graphite (HOPG) and the GaAs substrate, whose VBM values are determined to be 0.81 and 0.29 eV, respectively, by extrapolating a linear fit of the leading edge of the valence band photoemission to the baseline. Figure 3e, h reveal the binding energy of 284.74 eV for C 1*s* core level and 1118.56 eV for Ga 2*p* core level in the heterostructures treated with FLI. In order to further demonstrate the doping of Ga atoms into the graphene lattice, further XPS analysis results, of the high-resolution spectra of C1*s* core levels in a series of graphene/GaAs heterostructures treated with different laser power densities are presented in Supplementary Fig. 2, where the binding energy of 283.51 eV corresponding to the C–Ga bond is observed. This characteristic for C–Ga bonds has been reported by Lee et al.[34] and Maa and

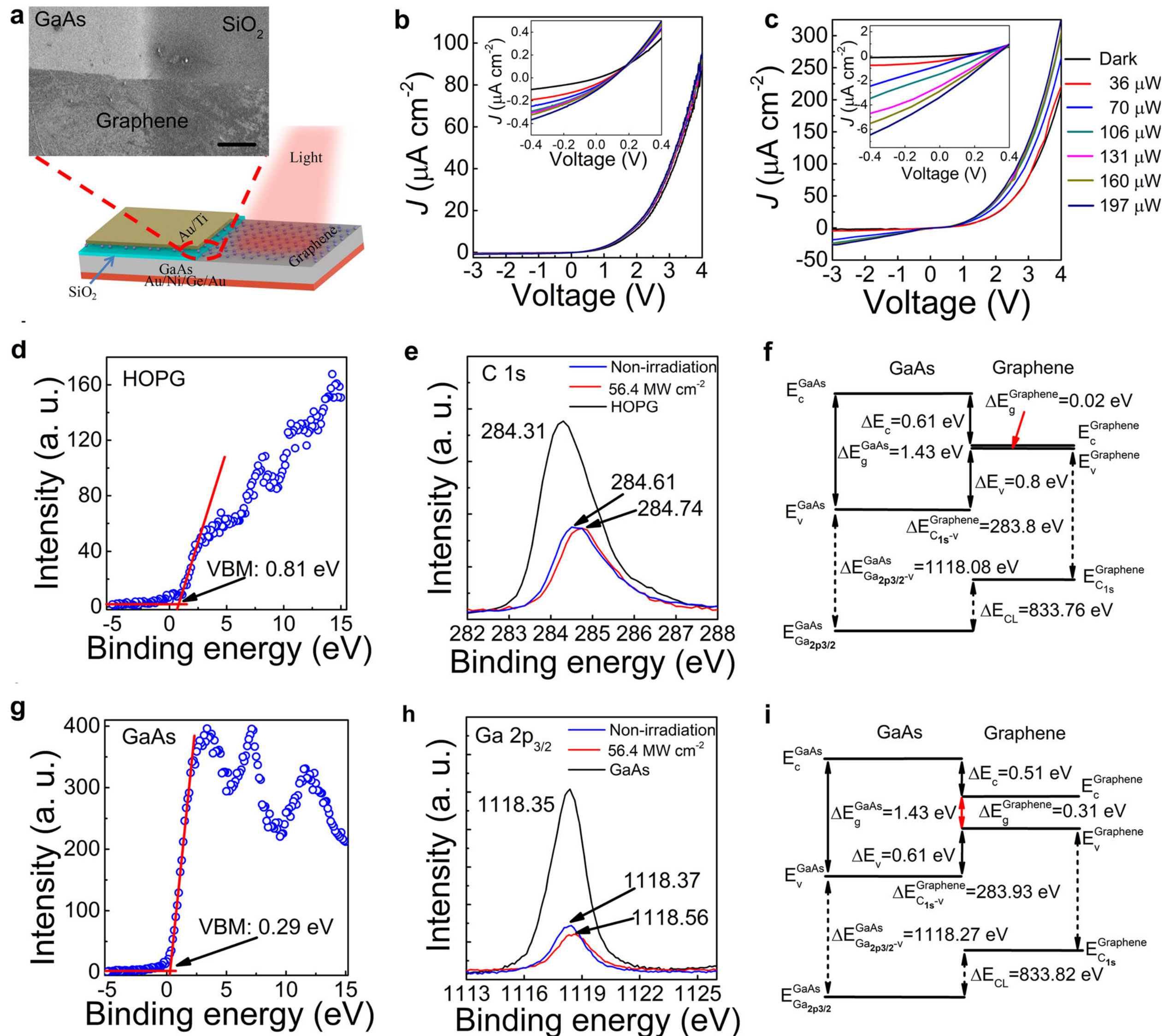

Fig. 3 Experimental signatures of photoresponse and XPS spectra. **a** Schematic of infrared photodetector based on a graphene/GaAs Schottky heterojunction, illuminated with the incident light of 1550 nm dispersed from a xenon lamp with a monochramator. Inset: a typical SEM image of graphene/GaAs Schottky heterojunction. The scale bar used is 100 μm. **b**, **c** Electrical characteristics of the non-FLI treated **b** and the FLI treated **c** graphene/GaAs heterojunctions measured at different illumination powers. **d**, **g** The FLI treatment was performed with the power density of 56.4 MW cm^{-2} at 740 nm from a femtosecond Ti:sapphire laser. Valence band spectra for **d** HOPG and **g** GaAs bulk. **e**, **h** High-resolution XPS spectra of **e** C1*s* and **h** Ga2*p* core levels for the irradiated and non-irradiated graphene/GaAs heterojunctions, HOPG, and GaAs bulk. **f**, **i** Band alignment diagram of the **f** non-irradiated and **i** irradiated graphene/GaAs heterojunctions.

Dapkus[35], which confirms that Ga atoms are doped into the graphene lattice and C–Ga bonds are created. The graphene in the femtosecond laser-irradiated heterostructure exhibits a much larger bandgap value of 0.31 eV compared to the non-irradiated structure, as illustrated by the band alignment diagrams depicted in Fig. 3f, i, which were obtained using the method referred in the "Methods" section. The parameters for calculating the band alignment of the graphene/GaAs heterostructures are listed in Supplementary Table 1. The calculated band structures of the monolayer graphene doped with respective Ga and As of the content varying in the range of 0.7–12.5% are shown in Supplementary Fig. 3. The Ga-doped graphene exhibits a bandgap ranging from 0.26 to 0.45 eV, while the As-doped graphene has a bandgap lower than 0.14 eV. We have found that the graphene bandgap in the graphene/GaAs heterostructure irradiated with 56.4 MW cm^{-2} is about 0.31 eV, which lies in the range of the calculated bandgap of the Ga-doped graphene, confirming the doping of Ga atoms into the graphene lattice. To exclude the influence of the water residues between the graphene and the GaAs on the bandgap opening of the graphene after the FLI, the atomic force microscopy (AFM) images of the graphene/GaAs heterostructure before and after the FLI are presented in Supplementary Fig. 4.

Optical properties of hybrid SAs

As depicted in Fig. 4a, InGaAs capped and SSL capped InAs QD SESAM structures were grown by molecular beam epitaxy (MBE) and a dot density of about 4×10^{10} cm^{-2} has been revealed by the AFM image. SA samples including graphene SAs, QD SAs, and hybrid SAs combining InAs QDs and graphene/GaAs heterostructures were fabricated. The test samples which had identical structures as to the SAs except for the bottom DBR were also prepared to allow comparison of PL spectra. Both the test samples and SAs were irradiated for 2 min with the Ti:sapphire laser at the

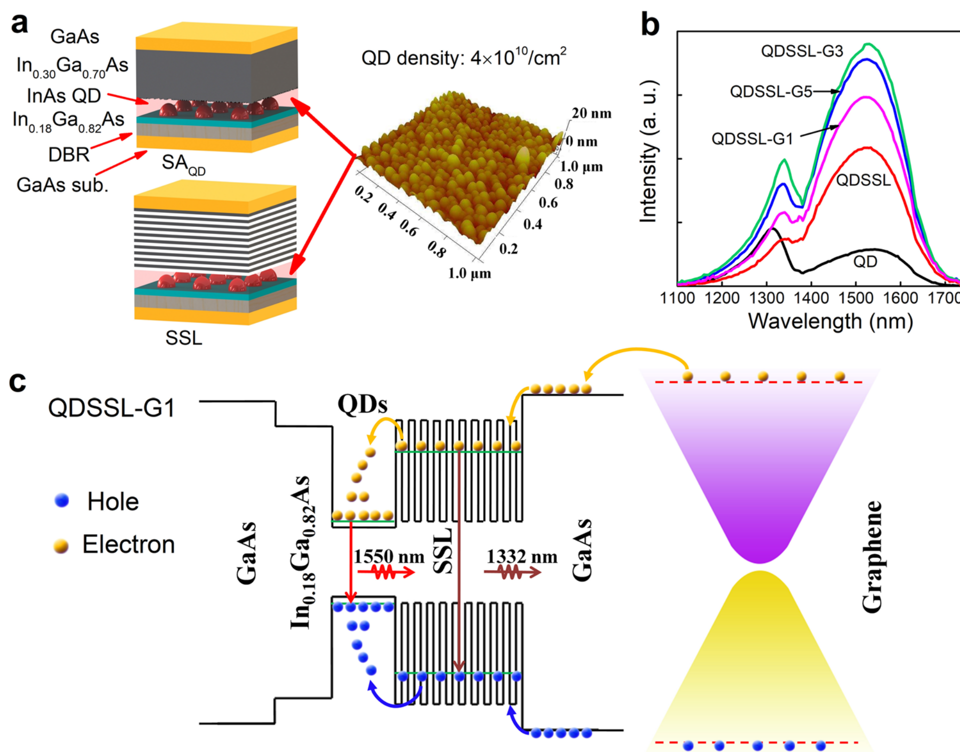

Fig. 4 Radiative recombination process of photo-generated carriers. **a** Schematic illustration of the SA_{QD} and SA_{QDSSL} structures as well as the AFM image of InAs QD layer. **b** PL spectra of test samples including $Test_{QD}$, $Test_{QDSSL}$, $Test_{QDSSL\text{-}G1}$, $Test_{QDSSL\text{-}G3}$, and $Test_{QDSSL\text{-}G5}$. **c** Energy band structures of the $Test_{QDSSL\text{-}G1}$ samples, depicting the carrier transfer and recombination processes accounting for the barrier emission at around 1332 nm and the QD emission at 1550 nm measured from the PL spectra.

average power density of 56.4 MW cm^{-2}. Figure 4b shows the PL spectra measured at room temperature with the excitation laser of 633 nm. All the samples exhibit two emission peaks corresponding to the capping and QD layers, respectively. A slight redshift of the 1332 nm emission peaks in the $Test_{QDSSL}$ sample can be observed, which can be attributed to the weaker quantum confinement effect of QW structure composed of the capping and GaAs layers due to the thicker SSL capping layer. Strikingly, the $Test_{QD}$ sample capped with InGaAs layers exhibits a weaker QD emission than the capping layer emission, while a much stronger QD emission than the capping layer is observed with the $Test_{QDSSL}$ sample capped by SSL layer. The main reason responsible for the enhanced QD PL emission lies in high-quality SSL capping layer with the uniform distribution of indium and the indium content decreased to 25%, which effectively modulates the carrier relaxation behaviors and enhances the capture of carriers by the QDs. Moreover, in the $Test_{QD}$ sample, it is harder for the photon-generated carriers to relax from the capping layer to the QDs, owing to the phonon bottleneck effect, which leads to much weaker radiative recombination of the carriers in QDs. In the case of $Test_{QDSSL}$, the carriers in the SSL structure tunnel across the SSL barriers, and experience much more scattering by the superlattice phonons[36], leading to greatly enhanced relaxation of the carrier energy and therefore improved carrier capture efficiency by the QDs. The $Test_{QDSSL\text{-}G1}$ sample ($Test_{QDSSL}$ sample coated with one layer of graphene) exhibits a much stronger PL emission than the $Test_{QDSSL}$ sample, which is believed to be due to the enhanced light harvesting by the graphene and the efficient carrier transfer from graphene to GaAs layer as depicted in Fig. 4c. A further increased PL intensity is observed for the $Test_{QDSSL\text{-}G3}$ sample coated with three layers of graphene, owing to further improved optical absorption by the multiple-layer graphene as described in Fig. 1f. However, due to the severe interface effects induced by the wet-chemical transfer of graphene, a weaker PL emission is observed in the sample with a five-layer graphene. Actually, more layers of graphene coating (i.e. 6, 7, and 8) have also been tried in our experiments, but the results show even poorer performance than the sample with five layers of graphene, which further confirms the severe interface effect in the multiple graphene layers structure achieved by wet-chemical transfer process. The PL enhancement effect and severe interface effect simultaneously happen in $Test_{QDSSL\text{-}G1}$, $Test_{QDSSL\text{-}G3}$, and $Test_{QDSSL\text{-}G5}$ samples. For $Test_{QDSSL\text{-}G1}$ and $Test_{QDSSL\text{-}G3}$ samples, the PL enhancement effect is dominant due to less number of interfaces in these samples. With the increase of the number of graphene layers, the interface effect becomes severe, even dominanting the PL enhancement effect and therefore leading to the decrease of the PL intensity in the $Test_{QDSSL\text{-}G5}$ sample.

SA properties and mode-locking characteristics

As described in Supplementary Fig. 5, the nonlinear saturable adsorption properties of the SAs were acquired with a typical balanced twin-detector setup[37]. The characteristics of the mode-locked EDF lasers measured with the representative SAs are listed in Supplementary Table 2. The obtained modulation depth of the SA_{QDSSL} is four times larger than that of the SA_{QD}, indicating the important impact of the SSL structure on the photon-generated carriers participating in the saturable absorption, i.e., the greatly enhanced carrier scattering and energy relaxation efficiency. In addition, as expected for the hybrid SAs with graphene/GaAs heterostructures, obviously increased modulation depth and decreased saturation intensity have been achieved. Taking the $SA_{QDSSL\text{-}G3}$ as an example, a saturation intensity <1/3 and a modulation depth 20 times greater than conventional SESAMs[38] have been obtained as shown in Fig. 5a and Supplementary Table 2. When the $SA_{QDSSL\text{-}G}$ is irradiated by a 1550 nm continuous wave or pulse laser, the electron–hole pairs are separated in graphene

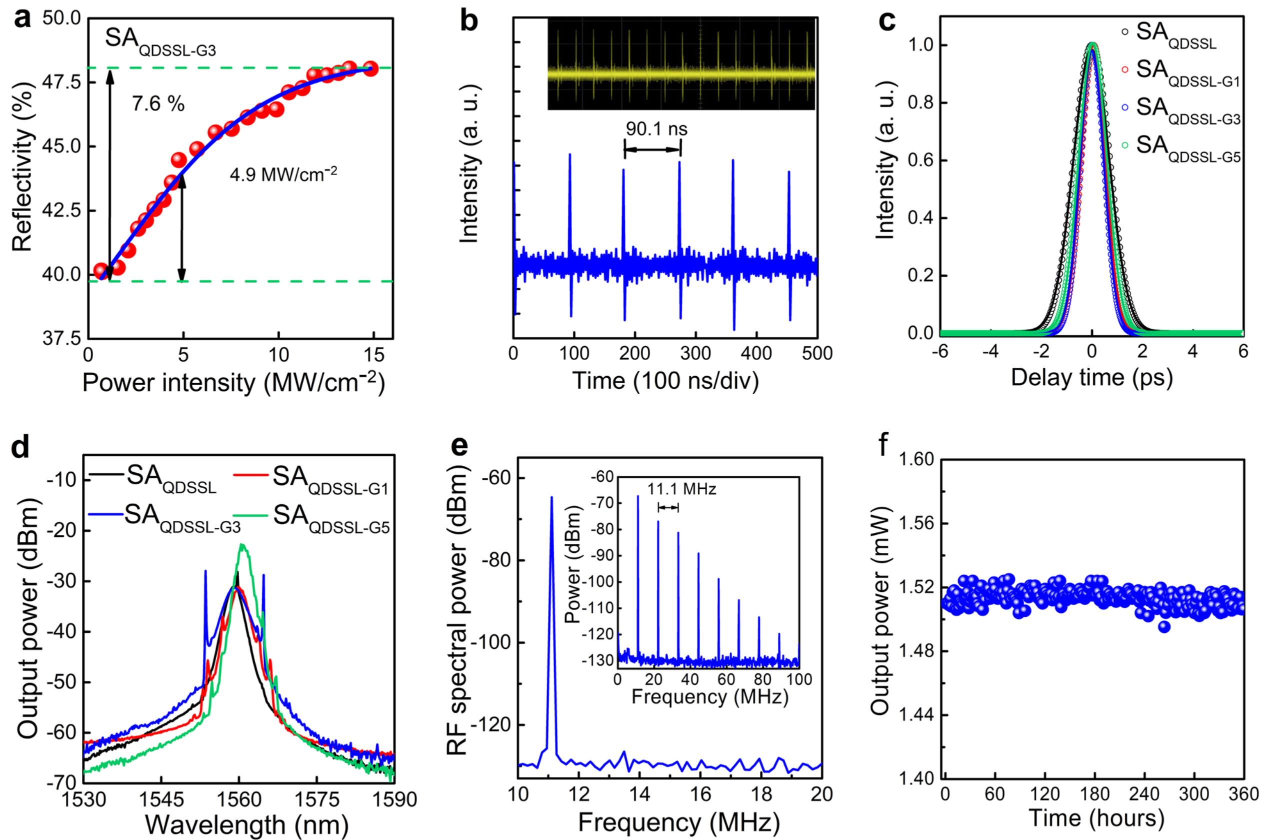

Fig. 5 Mode-locking characteristics. a Nonlinear reflection curves of irradiated $SA_{QDSSL-G3}$. **b** Mode-locking pulse train in the mode-locked laser based on irradiated $SA_{QDSSL-G3}$. **c** Autocorrelation trace of the optical pulse for the mode locking with irradiated SA_{QDSSL}, $SA_{QDSSL-G1}$, $SA_{QDSSL-G3}$, and $SA_{QDSSL-G5}$. **d** Mode-locked optical spectra of irradiated SA_{QDSSL}, $SA_{QDSSL-G1}$, $SA_{QDSSL-G3}$, and $SA_{QDSSL-G5}$. **e** RF spectra of mode locking with irradiated $SA_{QDSSL-G3}$. **f** Long-term stability measurement of mode locking with irradiated $SA_{QDSSL-G3}$.

and InAs QD layers. The generated electrons in the layer of graphene are transferred through the GaAs and SSL layers into the InAs QD layers, which effectively promote the bleaching process of SA. Therefore, the $SA_{QDSSL-G}$ sample exhibits lower saturation intensity than SA_{QDSSL}. Extensive work was carried out to demonstrate SESAMs as a mature and highly functional component in stable mode-locked lasers. However, obtaining a low saturation intensity and a large modulation depth simultaneously is challenging for conventional SESAM designs. Mode-locked fiber ring lasers in the configuration depicted in Supplementary Fig. 6 have been constructed with different SA samples and mode-locked behavior has been observed in all cases. Mode-locking pulse train in the mode-locked laser based on $SA_{QDSSL-G3}$ is shown in Fig. 5b. With the SA_{QDSSL} sample, the pulse width of ~1.1 ps is obtained, while a narrower pulse width of ~680 fs is observed with the $SA_{QDSSL-G3}$ sample at the central wavelength of 1559 nm with an associated bandwidth of 5.4 nm at 3 dB as shown in Fig. 5c, d. The radio frequency spectrum recorded at a span of 100 MHz is shown in Fig. 5e. The fundamental peak is located at 11.1 MHz, exhibiting a signal-to-noise ratio higher than 62 dB. Long-time stable mode-locking tests were carried out at a continuous pump current of 200 mA, and over 2 weeks stable operation was achieved. Figure 5f presents the result of the $SA_{QDSSL-G3}$ sample, revealing an almost unchanged output power over the extended time period, which is a crucial feature for practical applications.

High repetition rate pulse fiber lasers have attracted considerable attention due to the widely practical applications in fields such as fiber communication system and astronomical frequency combs. Harmonic mode locking of a fiber laser can be usually utilized to obtain high repetition rate pulse. As pump current increases from 295 to 600 mA, the harmonic pulse train of different orders (3rd, 11th, 18th, 21st, 27th, and 34th) with the span of 70 ns are obtained by employing the irradiated $SA_{QDSSL-G3}$, as shown in Fig. 6a, respectively. At the same time, the output power increases from 2.1 to 7 mW and the repetition rate of the harmonic mode locked fiber laser gradually increases from 33.3 to 377.4 MHz (34th harmonic of fundamental repetition frequency), as shown in Fig. 6b–d. Moreover, the long time stable of harmonic mode-locked pules can also be observed at different pump powers. The stable 377.4 MHz harmonic mode-locked fiber laser based on the irradiated $SA_{QDSSL-G3}$, indicating these hybrid SESAMs have great potential in optical communication systems.

DISCUSSION

In this work, we have demonstrated the enhancement of both the photon harvesting and carrier transfer efficiencies in the graphene/III–V semiconductor vdW heterostructure due to the bandgap opening of graphene induced by the method of FLI. To verify the carrier transfer characteristics and bandgap opening of graphene, SIP devices were fabricated by transferring the graphene onto a GaAs substrate. The measured photocurrent density of the SIP device irradiated with a Ti:sapphire femtosecond pulsed laser at power density of 56.4 MW cm^{-2} is 20 times larger than the non-irradiated device, which can be ascribed to the bandgap opening of 0.31 eV in graphene due to the FLI-induced C and Ga atoms exchange at the graphene/III–V semiconductor. Fully benefitting from the bandgap opening of graphene, we have developed a SA combining a delicately engineered graphene/GaAs vdW heterostructure with InAs QDs capped with SSLs. By controlling the layer number of graphene, the saturation intensity is tuned from 3.3 to 13.7 MW cm^{-2} and the modulation depth is

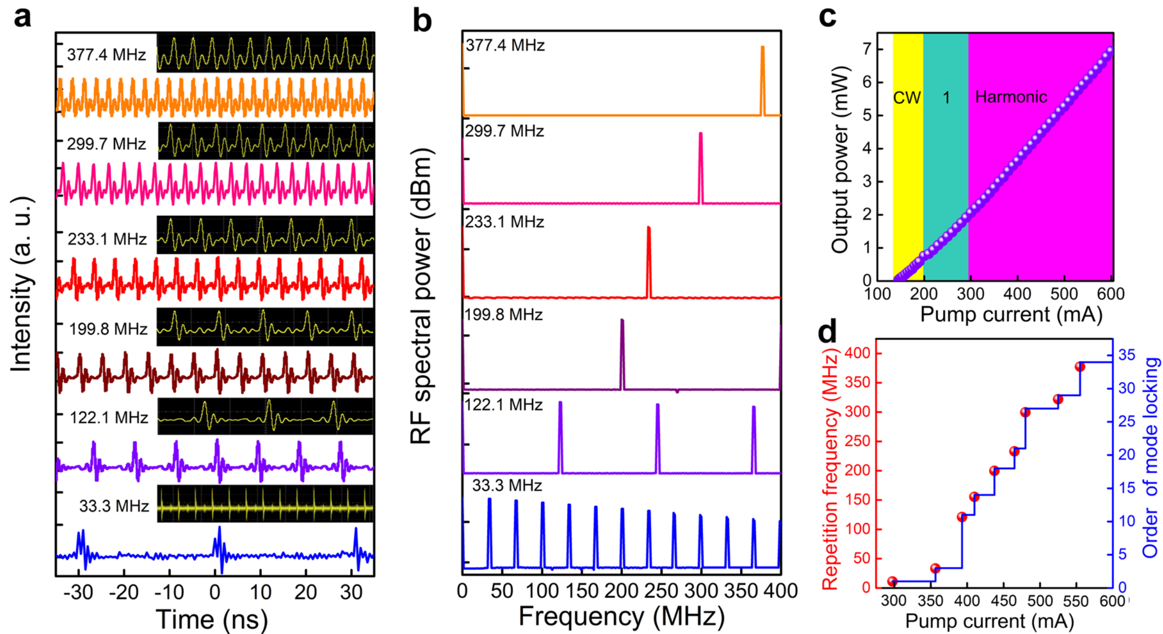

Fig. 6 Harmonically mode-locked fiber laser. a Harmonic pulse evolution of different orders. **b** RF spectra of different orders harmonic pulse. **c** Output average power versus pump power. **d** Repetition rate and orders of mode locking versus the pump power.

adjusted from 1.6% to 9.9%. Using these hybrid SAs, we finally constructed a 1.55 μm mode-locked ultrafast fiber laser which exhibits a pulse width of 680 fs and continuously stable mode-locking for more than 2 weeks. Our finding can be applicable not only to improve the performance of SESAM working at other wavelength, but also to other types of optoelectronic devices based on graphene/III–V semiconductor vdW heterostructures, such as light-emitting diodes and photo-detectors, which therefore expands both theoretical and experimental research fields of hybrid vdW-based device applications.

METHODS

MBE growth of the SESAM structures

Two QD SESAM samples comprising a single QD absorption layer and a bottom GaAs/AlGaAs DBR were grown with solid-source MBE, which have an asymmetric DWELL structure with different types of capping layers. As shown in Fig. 4a, the InAs QDs in the SA_{QD} sample were grown on 1 nm $In_{0.18}Ga_{0.82}As$ layer with a capping layer of 6 nm $In_{0.30}Ga_{0.70}As$, while SA_{QDSSL} was capped with a 10 nm $(In_xGa_{1-x}As/\ In_yGa_{1-y}As)_n$ SSL layer, with an average In % of ~25%. The high-quality SSL capping layer with uniform distribution of indium can effectively modulate the carrier relaxation behaviors and enhance the capture of carriers by the QDs, which is the main factor responsible for the enhanced QD PL emission.

Fabrication of graphene/GaAs SIP device

Before wet-chemical transfer process of graphene, a 200 nm SiO_2 layer was deposited on the thinned semi-insulation (SI)-GaAs substrate by using plasma-enhanced chemical vapor deposition method as shown in Fig. 3a. Then, graphene film was transferred to the SiO_2/SI-GaAs substrate. The water bubbles in the graphene and SiO_2/SI-GaAs interface were removed by slow air blowing. After that, two rectangle metal electrodes including a Ti/Au electrode with an area of 0.04 cm^2 and an Au/Ni/Ge/Au electrode with an area of 0.1 cm^2 were deposited to form the top and bottom ohmic contacts, respectively.

Calculations of band alignment for graphene/GaAs heterostructure

One of the key parameters in designing a heterojunction is the band offset which is critical for the transfer behaviors of the photo-generated carriers. To gain insight into the electronic structure of the irradiated and non-irradiated graphene/GaAs interfaces, high-resolution XPS analysis was performed and the spectra of the valence bands, C_{1s} and $Ga_{2p3/2}$ core levels were all measured on HOPG, the GaAs substrate, and the irradiated and non-irradiated graphene/GaAs heterostructures. Figure 3d, g show the valence band spectra of HOPG and the GaAs substrate, whose VBM values are determined to be 0.81 and 0.29 eV, respectively, by extrapolating a linear fit of the leading edge of the valence band photoemission to the baseline. The C1*s* spectra for HOPG and the non-irradiated graphene/GaAs heterostructure are shown in Fig. 3e, revealing the binding energies of 284.31 and 284.61 eV, respectively. The Ga 2*p* spectra in Fig. 3h exhibit the binding energies of 1118.35 and 1118.37 eV for the GaAs substrate and the non-irradiated graphene/GaAs heterostructure, respectively. The valence band offset (VBO) of the graphene/GaAs heterostructure can be determined according to the relation[39]:

$$\Delta E_v = \Delta E_{CL} + (E_{VBM}^{HOPG} - E_{C_{1s}}^{HOPG}) - (E_{VBM}^{GaAs} - E_{Ga_{2p3/2}}^{GaAs}), \quad (1)$$

where ΔECL is the difference in the binding energy between Ga 2*p* and C 1*s* core levels at the non-irradiated graphene/GaAs interface, and $(E_{VBM}^{HOPG} - E_{C_{1s}}^{HOPG})$ and $(E_{VBM}^{GaAs} - E_{Ga_{2p3/2}}^{GaAs})$ are the valence band maxima (VBM) energies with reference to the core level peaks in the single layer graphene and the GaAs substrate, respectively. Moreover, the bandgap ($\Delta E_g^{Graphene}$) of the graphene transferred onto the GaAs substrate can be estimated by the formula[39]:

$$\Delta E_g^{Graphene} = E_g^{GaAs} - \Delta E_v - \Delta E_c \quad (2)$$

By using the room-temperature bandgap value (E_g^{GaAs}) of 1.43 eV, $\Delta E_g^{Graphene}$ is calculated to be 0.02 eV. As a result, the schematic band alignment diagram of the graphene/GaAs heterostructure is depicted in Fig. 3f.

Femtosecond laser-induced doping treatment

The graphene/GaAs vdW heterostructures studied in this work were fabricated by wet-chemical transfer of graphene layers onto GaAs surface and then were irradiated for 2 min with a femtosecond Ti:sapphire laser (center wavelength: 740 nm, pulse duration: 130 fs, repetition rate: 76 MHz). The power density employed for the FLI treatment is in the range of 0–70.3 MW cm^{-2}.

DATA AVAILABILITY

The datasets generated during and/or analyzed during the current study are available from the corresponding author on reasonable request. All data generated or

analyzed during this study are included in this published article (and its Supplementary Information).

Received: 25 February 2020; Accepted: 15 July 2020;
Published online: 31 July 2020

REFERENCES

1. Kurman, Y. et al. Control of semiconductor emitter frequency by increasing polariton momenta. *Nat. Photon.* **12**, 423–429 (2018).
2. Jariwala, D., Marks, T. J. & Hersam, M. C. Mixed-dimensional van der Waals heterostructures. *Nat. Mater.* **16**, 170–181 (2017).
3. Sun, M. et al. Tunable schottky barrier in van der Waals heterostructure of grapheme and g-GaN. *Appl. Phys. Lett.* **110**, 173105 (2017).
4. Novoselov, K. S., Mishchenko, A., Carvalho, A. & Neto, A. H. 2D materials and van der Waals heterostructures. *Science* **353**, aac9439 (2016).
5. Choi, K., Lee, Y. T. & Im, S. Two-dimensional van der Waals nanosheet devices for future electronics and photonics. *Nano Today* **5**, 626–643 (2016).
6. Li, X. et al. 18.5% efficient graphene/GaAs van der Waals heterostructure solar cell. *Nano Energy* **16**, 310–319 (2015).
7. Gamucci, A. et al. Anomalous low-temperature Coulomb drag in grapheme-GaAs heterostructures. *Nat. Commun.* **5**, 5824 (2014).
8. Kim, Y. S. et al. Direct integration of polycrystalline graphene into light emitting diodes by plasma-assisted metal-catalyst-free synthesis. *ACS Nano* **8**, 2230 (2014).
9. Geim, A. K. & Grigorieva, I. V. Van der Walls heterostructures. *Nature* **499**, 419–425 (2013).
10. Han, N. et al. Improved heat dissipation in gallium nitride light-emitting diodes with embedded graphene oxide pattern. *Nat. Commun.* **4**, 1452 (2013).
11. Sinitskii, A. A recipe for nanoporous graphene. *Science* **360**, 154–155 (2018).
12. Zeng, Y. et al. Highly enhanced photoluminescence of monolayer MoS_2 with self-assembled Au nanoparticle arrays. *Adv. Mater.* **4**, 1700739 (2017).
13. Bao, Q. et al. Atomic-layer graphene as a satureable absorber for ultrafast pulsed laser. *Adv. Funct. Mater.* **19**, 3077–3083 (2009).
14. Liu, J. Y. et al. Switchable dual-wavelength Q-switched fiber laser using multilayer black phosphorus as a saturable absorber. *Photonics Res.* **6**, 198–203 (2018).
15. He, X. Y., Zhang, X. C., Zhang, H. & Xu, M. Graphene covered on microfiber exhibiting polarization and polarization-dependent saturable absorption. *IEEE J. Sel. Top. Quant.* **20**, 4500107 (2014).
16. Arakawa, Y. & Sakaki, H. Multidimensional quantum well laser and temperature dependence of its threshold current. *Appl. Phys. Lett.* **40**, 939–941 (1982).
17. Li, Q. et al. Development of modulation p-doped 1310 nm InAs/GaAs quantum dot laser materials and ultrashort cavity Fabry–Perot and distributed-feedback laser diodes. *ACS Photonics* **5**, 1084–1095 (2018).
18. Chen, S. et al. Electrically pumped continuous-wave III–V quantum dot lasers on silicon. *Nat. Photon.* **10**, 307–311 (2016).
19. Liang, D. & Bowers, J. E. Recent progress in lasers on silicon. *Nat. Photon.* **4**, 511–517 (2010).
20. Rafailov, E. U., Cataluna, M. A. & Sibbett, W. Mode-locked quantum-dot lasers. *Nat. Photon.* **1**, 395–401 (2007).
21. McWilliam, A. et al. Quantum-dot-based saturable absorber for femtosecond mode-locked operation of a solid-state laser. *Opt. Lett.* **31**, 1444–1446 (2006).
22. Keller, U. Recent developments in compact ultrafast lasers. *Nature* **424**, 831–838 (2003).
23. Wang, X. et al. InAs/GaAs quantum dot semiconductor saturable absorber for controllable dual-wavelength passively Q-switched fiber laser. *Opt. Express* **27**, 20649 (2019).
24. Zhang, Z. Y. et al. 1.55 µm InAs/GaAs quantum dots and high repetition rate quantum dot SESAM mode-locked laser. *Sci. Rep.* **2**, 477 (2012).
25. Tan, Y. et al. Tuning of interlayer coupling in large-area graphene/WSe_2 van der Waals heterostructure via Ion Irradiation: optical evidences and photonic applications. *ACS Photonics* **4**, 1531–1538 (2017).
26. Resan, B. et al. 10 GHz pulse repetition rate Er: Yb: glass laser modelocked with quantum dot semiconductor saturable absorber mirror. *Appl. Opt.* **55**, 3776–3780 (2016).
27. Gao, F. et al. Ultrashort pulse and high power mode-locked laser with chirped InAs/InP quantum dot active layers. *IEEE Photon. Technol. Lett.* **28**, 1481–1484 (2016).
28. Renaudier, J. et al. Duan, standard-compliant jitter transfer function of all-optical clock recovery at 40 GHz based on a quantum-dot self-pulsating semiconductor laser. *IEEE Photon. Technol. Lett.* **18**, 1249–1251 (2006).
29. Holman, K. W. et al. Orthogonal control of the frequency comb dynamics of a mode-locked laser diode. *Opt. Lett.* **28**, 2405–2407 (2003).
30. Das, A. et al. Monitoring dopants by Raman scattering in an electrochemically top-gated graphene transistor. *Nature* **3**, 201 (2008).
31. Kar, S. et al. Tuning photoinduced terahertz conductivity in monolayer graphene: Optical-pump terahertz-probe spectroscopy. *Phys. Rev. B* **90**, 165420 (2014).
32. Maultzsch, J., Reich, S. & Thomsen, C. Double-resonant Raman scattering in graphite: Interference effects, selection rules, and phonon dispersion. *Phys. Rev. B* **70**, 155403 (2004).
33. Wang, W. et al. High-performance position-sensitive detector based on graphene–silicon heterojunction. *Optica* **5**, 27–31 (2018).
34. Lee, F. et al. Decomposition of trimethylgalliun on Si (100): spectroscopic identification of the intermediates. *Surf. Sci.* **216**, 173–188 (1989).
35. Maa, B. & Dapkus, P. RHEED and XPS observations of trimethylgalliun adsorption on GaAs (001) surfaces-relevance to atomic layer epitaxy. *J. Electron. Mater.* **19**, 289–294 (1990).
36. Inoshita, I. & Sakaki, H. Electrom relaxation in a quantum dot: significance of multiphonon processes. *Phys. Rev. B* **46**, 7260–7263 (1992).
37. Mao, D. et al. Nonlinear saturable absorption of liquid-exfoliated moltbdenum/tungsten ditelluride naosheets. *Small* **11**, 1489–1497 (2016).
38. Spühler, G. J. et al. Semiconductor saturable absorber mirror structures with low saturation fluence. *Appl. Phys. B* **81**, 27–32 (2005).
39. Karamat, S. et al. Graphene/$SrTiO_3$ heterointerface studied by X-ray photoelectron spectroscopy. *PNS:MI* **26**, 422–426 (2016).

ACKNOWLEDGEMENTS

We acknowledge Natural Science Foundation of China (Grant Nos. 61875222, 61875223, 61605106, 11874390). We thank the Nanofabrication facility for device fabrication and characterization in Suzhou Institute of Nano-Tech and Nano-Bionics, Chinese Academy of Sciences.

AUTHOR CONTRIBUTIONS

Z.Y.Z. conceived the original idea. Z.Y.Z., C.T.A.B., and J.Q.N. supervised the project. X.W. and X.H.L. carried out the materials and devices characterizations. Z.Y.Z. grew the QD-SESAMs, and X.W, Q.Y. and C.J. made the graphene-coating process. X.W., X.T.G., and J.Q.N. performed the laser irradiation annealing process and photoresponse characterization. X.W. performed the XPS measurements. X.W. and C.J. finalized the schematic images. All authors helped in analyzing and interpreting the data. Z.Y.Z., C.T.A.B., J.Q.N., X.W., X.H.L., and Q.J.W. wrote the paper and all authors commented on it.

COMPETING INTERESTS

The authors declare no competing interests.

ADDITIONAL INFORMATION

Supplementary information is available for this paper at https://doi.org/10.1038/s41699-020-00160-6.

Correspondence and requests for materials should be addressed to Z.Y.Z.

Reprints and permission information is available at http://www.nature.com/reprints

Publisher's note Springer Nature remains neutral with regard to jurisdictional claims in published maps and institutional affiliations.

Open Access This article is licensed under a Creative Commons Attribution 4.0 International License, which permits use, sharing, adaptation, distribution and reproduction in any medium or format, as long as you give appropriate credit to the original author(s) and the source, provide a link to the Creative Commons license, and indicate if changes were made. The images or other third party material in this article are included in the article's Creative Commons license, unless indicated otherwise in a credit line to the material. If material is not included in the article's Creative Commons license and your intended use is not permitted by statutory regulation or exceeds the permitted use, you will need to obtain permission directly from the copyright holder. To view a copy of this license, visit http://creativecommons.org/licenses/by/4.0/.

© The Author(s) 2020